The Astrophysical Journal, 899:151 (15pp), 2020 August 20 https://doi.org/10.3847/1538-4357/aba1e9

Exploring the Acceleration Mechanisms for Particle Injection and Power-law Formation during Transrelativistic Magnetic Reconnection

Patrick Kilian[1,2], Xiaocan Li[3], Fan Guo[1,4], and Hui Li[1]
[1] Los Alamos National Laboratory, Los Alamos, NM 87545, USA; pkilian@lanl.gov
[2] Centre for Space Research, North-West University, Potchefstroom, South Africa
[3] Dartmouth College, Hanover, NH 03750, USA
[4] New Mexico Consortium, Los Alamos, NM 87544, USA
Received 2020 January 8; revised 2020 June 29; accepted 2020 June 30; published 2020 August 25

Abstract

Magnetic reconnection in the relativistic and transrelativistic regimes is able to accelerate particles to hard power-law energy spectra $f \propto \gamma^{-p}$ (approaching $p = 1$). The underlying acceleration mechanism that determines the spectral shape is currently a topic of intense investigation. By means of fully kinetic plasma simulations, we carry out a study of particle acceleration during magnetic reconnection in the transrelativistic regime of a proton–electron plasma. While earlier work in this parameter regime has focused on the effects of electric field parallel to the local magnetic field on the particle injection (from thermal energy to the lower-energy bound of the power-law spectrum), here we examine the roles of both parallel and perpendicular electric fields to gain a more complete understanding on the injection process and further development of a power-law spectrum. We show that the parallel electric field does contribute significantly to particle injection, and is more important in the initial phase of magnetic reconnection. However, as the simulation proceeds, the acceleration by the perpendicular electric field becomes more important for particle injection and completely dominates the acceleration responsible for the high-energy power-law spectrum. This holds robustly, in particular for longer reconnection times and larger systems, i.e., in simulations that are more indicative of the processes in astrophysical sources.

Unified Astronomy Thesaurus concepts: Non-thermal radiation sources (1119); Magnetic fields (994)

1. Introduction

Magnetic reconnection is the process that changes magnetic-field topology. This requires at least a local violation of the frozen-flux theorem. In typical astrophysical, collisionless plasmas this happens due to kinetic, microphysical processes. Once the magnetic field lines are broken and reconnected, the magnetic field in its new topology relaxes to a lower-energy configuration at much larger scales. The released energy in converted into heating, bulk flows, and a tail of high-energy particles (Zelenyi et al. 1990; Zenitani & Hoshino 2001; Guo et al. 2014). This source of nonthermal particles is thought to be important in a number of high-energy astrophysical environments such as pulsar wind nebulae, gamma-ray bursts, and jets from active galactic nuclei. Knowing the process of particle acceleration is important for making predictions of the particle energy spectra.

Past research on particle acceleration during magnetic reconnection has mainly explored two mechanisms: Fermi-type acceleration where particles are accelerated by bouncing back and forth in the reconnection generated flows (de Gouveia dal Pino & Lazarian 2005; Drake et al. 2006; Fu et al. 2006; Drury 2012; Dahlin et al. 2014; Guo et al. 2014; le Roux et al. 2015; Li et al. 2018a, 2018b, 2019), and direct acceleration at diffusion regions surrounding reconnection X-points (Zenitani & Hoshino 2001; Pritchett 2006; Cerutti et al. 2013; Sironi & Spitkovsky 2014; Wang et al. 2016). The Fermi-type acceleration is mainly through the electric field induced by bulk plasma motion $\boldsymbol{E}_m = -\boldsymbol{u} \times \boldsymbol{B}/c$ perpendicular to the local magnetic field, whereas the direct acceleration is driven by the parallel electric field if a non-zero magnetic field exists. It is therefore useful to distinguish the relative contribution of the two during the particle acceleration process, either according to the generalized Ohm's law (Guo et al. 2019), or simply by decomposing the electric field into the perpendicular part $E_\perp$ and parallel component $E_\parallel$ and evaluating the work done by each of them (Guo et al. 2015; Ball et al. 2019).

Since the magnetic field is the source of free energy for these energization processes, it is useful to define two parameters that compare the magnetic field with other characteristic properties of the plasma. The first parameter is the magnetization $\sigma = B_0^2/(4\pi\rho c^2)$, where B_0 is the magnetic field strength, ρ is mass density, and c is the speed of light. This ratio between energy density in the magnetic field to the energy density associated with the rest mass of the particles can also be seen as the energy available per particle from the magnetic field if the magnetic energy was fully converted through reconnection. The second parameter is the plasma β defined as $\beta = 8\pi n k_B T/B_0^2$. This ratio compares the thermal pressure of the gas with the pressure due to the magnetic field. Alternatively, this can be expressed by $\sigma_{\rm th} = B_0^2/(12\pi n k_B T) = 2/(3\,\beta)$, the ratio between magnetic field energy and thermal energy density that measures the maximum possible energization per particle compare with the thermal energy.

Magnetic reconnection is especially interesting in the case of $\beta \lesssim 1$ since more energy is available for particle energization. The nonrelativistic case of $\sigma \ll 1$ of magnetic reconnection has been studied for many years (Zelenyi et al. 1990; Biskamp 1996; Birn et al. 2001; Hesse et al. 2001; Priest & Forbes 2007; Shay et al. 2007; Treumann & Baumjohann 2013; Muñoz et al. 2015; Li et al. 2018a, 2019). This parameter regime is especially relevant to space and solar physics and is accessible in laboratory experiments. More recently (ultra-)relativistic reconnection with $\sigma \gg 1$ has also been studied (Zenitani & Hoshino 2001; Lyubarsky & Liverts 2008; Guo et al. 2014, 2015, 2016; Sironi & Spitkovsky 2014;

Liu et al. 2015, 2017, 2020; Werner et al. 2015). This parameter regime is of particular interest in astrophysics, such as jets from active galactic nuclei or pulsar magnetospheres. In these systems σ is so large that, even if only a small fraction of the magnetic energy is released, particles can still reach relativistic energies. Simulations show that the resulting particle distribution functions often have hard power-law tails that extend to large Lorentz factors (Guo et al. 2014, 2015, 2016; Sironi & Spitkovsky 2014; Werner et al. 2015). These particle spectra might be responsible for observed high-energy emission through inverse-Compton upscatter of softer seed photons, synchrotron radiation from the gyration of the energetic particles in the magnetic field, or other processes such as Bremsstrahlung.

In recent years the transrelativistic regime $\sigma \approx 1$ has generated interest as well (Melzani et al. 2014a, 2014b; Rowan et al. 2017, 2019; Werner et al. 2017; Ball et al. 2018, 2019). One particularity of this regime is that the available energy compared to the rest mass of ions $\sigma_i = B_0^2/(4\pi\rho_i c^2)$ is around unity ($\sigma_i \approx 1$, where $\rho_i = m_i\, n_i$ is the mass density of ions with mass per ion of m_i and number density n_i). For electrons with mass m_e and number density $n_e \approx n_i$, ,however $\sigma_e = B_0^2/(4\pi\rho_e c^2) \gg 1$. When magnetic field energy is converted, this leads to only mildly relativistic ions but a fraction of electrons can be very relativistic.

One astrophysical class of objects where $\sigma \approx 1$, $\beta \lesssim 1$ is thought to occur are radiatively inefficient, geometrically thick, optically thin accretion disks around black holes that accrete much less then their Eddington limit. Even in disks that accrete more rapidly this condition might be satisfied in the corona above the disk (di Matteo 1998). Simulations of magnetohydrodynamics that include effects of general relativity (GRMHD) give a sense of the overall flow geometry and energy contained in radiation, magnetic fields, and ion fluid (Chan et al. 2015; Porth et al. 2017; Davelaar et al. 2018; Chael et al. 2019; Mahlmann et al. 2020; Nathanail et al. 2020). The energy content in the electrons is basically unconstrained by single-fluid simulations, but is of importance for predictions of observable electromagnetic signatures, since the electrons radiate away their energy much more readily. It is therefore interesting to study the process of electron energization in much more detail.

Rowan et al. (2017) concentrated on the heating of electrons and ions and the temperature ratio T_e/T_i. They also investigated the artificial influence of the numerical mass ratio m_i/m_e. Simulations with full mass ratios are possible and preferable, as simulations with small mass ratios can overestimate the heating rate. Above the energies found in the heated distribution, the particle spectrum tends to form a power law with an exponential cutoff $f(\gamma) \propto \gamma^{-p}\exp(\gamma/\gamma_c)$. In Werner et al. (2017) the scaling of p and γ_c with magnetization σ is studied in the range $\sigma_i = 0.03...10^4$ and an empirical fit formula is provided. The authors also investigate the energy partition between electrons and protons. They find that toward the nonrelativistic regime electrons only receive about one-fourth of the energy, but electrons and protons obtain equal amounts of energy as σ_i gets larger.

In Ball et al. (2018) a similar study is performed for $\sigma = 0.3...3$, but additionally the dependence on β in the range $10^{-4}...1.5$ is investigated. The paper also investigates the role of X-point acceleration and Fermi acceleration and presents some resulting particle trajectories and spectra. Ball et al. (2019) continues the particle acceleration study and focuses on the question of how particles get into the power-law tail of the energy distribution. To this end the authors select a Lorentz factor $\gamma_{\rm inj} = \sigma_e/2$ that separates the low-energy part of the energy distribution from the power-law tail in their simulations with $\sigma_i = 0.3$. The analysis is mostly limited to the role of $W_{\parallel}$ and how and where particles cross $\gamma_{\rm inj}$.

In this paper, we extend this analysis and investigate the role of both the parallel and perpendicular electric fields where the directions are defined with respect to the local magnetic field. To ensure that our results can be readily compared with Ball et al. (2019) we chose identical parameters wherever feasible. The only difference is the choice of initial equilibrium (we chose a force-free current sheet instead of a Harris sheet) and the form of initial perturbation (we perturb the magnetic field instead of a localized reduction in thermal pressure). However, we believe the two simulations are sufficiently similar for comparison. We do, however, limit our investigation to the triggered case and only consider $B_g = 0.1B_0$, omitting the case of $B_g = 0.3B_0$. The effects of the guide field will be discussed in a forthcoming study. We find that the parallel electric field does accelerate a fraction of electrons to the injection energy in the initial phase of reconnection. However, as reconnection proceeds, the acceleration by the perpendicular electric field becomes important and outperforms the parallel electric field for particle injection. Moreover, the acceleration from the injection energy into power-law energies is completely dominated by the perpendicular electric field. The resulting power-law index does not seem to strongly depend on the injection mechanism. These findings provide further evidence for the roles of the Fermi-like process in determining particle acceleration into a power-law spectrum during magnetic reconnection.

The remainder of the paper is organized as follows. In Section 2 we describe the simulation code and the initial setup that results in magnetic reconnection in the desired transrelativistic regime. In Section 3 the results obtained from the simulation are described. In Section 4 we discuss and draw conclusions on the relative roles of the parallel and perpendicular electric fields.

2. Simulation Setup

To study the processes involved in electron energization we perform fully kinetic simulations using the VPIC code by Bowers et al. (2008a, 2008b, 2009). The code uses a relativistically correct implementation of the Boris push (Boris 1970) to move macroparticles that represent phase-space density and interpolates to and from the Eulerian grid using a low-order, energy-conserving scheme. The current deposition is constructed such that the continuity equation between particles' charges and currents on the grid is satisfied. Additionally, deviations from Gauss's Law are cleaned periodically to prevent round-off errors from accumulating. The electromagnetic fields on the grid are advanced using a standard Yee scheme (Yee 1966).

Inside the code we set up a single force-free current sheet in the electron–proton plasma with natural mass ratio $m_i/m_e = 1836$. We choose a force-free current sheet instead of a Harris current sheet, as this removes the arbitrary choice of overdensity η inside the current sheet compared to the upstream plasma. To remove any influence of this choice on the analysis results, we show results including and excluding the particles

that start inside the current sheet in the analysis below. Our two-dimensional simulation resolves the x and z directions, where the x direction is along the upstream magnetic field and the magnetic field direction varies with the z direction across the current sheet. The x direction has periodic boundary conditions on particles and fields. The z direction is terminated by fixed walls at the top and bottom of the domain. These walls are electrically perfectly conducting and flip the v_z velocity component of particles hitting the wall. This way the z boundaries reflect electromagnetic waves as well as particles. There is no inflow of plasma or magnetic flux from the z direction and the reconnection exhaust eventually interacts with each self across the periodic x boundary. This terminates reconnection eventually, as discussed below. We do include a guide field B_g that is perpendicular to the anti-parallel reconnecting magnetic field B_0. In the upstream this field is in the out-of-plane direction and has strength $B_g = 0.1B_0$. The initial field configuration is given by

$$B_x = B_0 \tanh(z/\lambda) + \delta B_x, \tag{1}$$

$$B_y = B_0 \sqrt{(B_g/B_0)^2 + \mathrm{sech}^2(z/\lambda)}, \tag{2}$$

$$B_z = \delta B_z. \tag{3}$$

This magnetic field has constant magnitude $\sqrt{B_0^2 + B_g^2}$ and rotates through an angle $\pi - 2\arctan B_g/B_0 \approx 169°$ when crossing the current sheet in the z direction. In terms of the electron skin depth $d_e = c/w_{pe}$ the characteristic thickness of the initial current sheet is $\lambda = 14.1\, d_e$. Reconnection is triggered by a divergence-free, long-wavelength perturbation that is described by

$$\delta B_x = -\frac{L_x B_0}{100 L_z} \cos\left(\frac{2\pi(x - 0.5L_x)}{L_x}\right) \sin\left(\frac{\pi z}{L_z}\right),$$

$$\delta B_z = \frac{B_0}{50} \sin\left(\frac{2\pi(x - 0.5L_x)}{L_x}\right) \cos\left(\frac{\pi z}{L_z}\right).$$

We primarily discuss the case where the size of the simulation domain is $L_x \times L_y \times L_z = 2720\, d_e \times 0.33\, d_e \times 1360\, d_e$ and is resolved by $N_x \times N_y \times N_z = 8192 \times 1 \times 4096$ grid cells. In addition, we have explored the effects of the box sizes and results are summarized in Appendix A. The time step was set to $\Delta t = 0.188\omega_{pe}^{-1}$, 80% of the maximum time step permitted by the CFL condition. Ions and electrons are each represented by 100 particles per cell. Our choice of $\sigma_i = 0.3$ sets the plasma density and implies $\sigma_e \approx 552.5$. Together with the mass ratio this also sets $\omega_{pe}/\Omega_{ci} = 78.1$. The initial plasma temperature is given by $k_B T_e = k_B T_i = 0.918\, m_e c^2$. The plasma beta resulting from these parameters is $\beta = 3.3 \times 10^{-3}$, $\sigma_{th} = B_0^2/(12\pi n k_B T) = 2/(3\beta) \approx 200$.

To analyze the particle acceleration process, a small fraction of the macroparticles—0.67 million electrons—are randomly selected in the beginning of the simulation and designated as tracer particles. For these particles quantities of interest such as the work done by the electric field and the parallel and perpendicular components $E_\parallel$ and $E_\perp$ is computed in every time step and is output for later analysis.

3. Results

As expected, the perturbed equilibrium is unstable and quickly starts to reconnect at the induced X-point and secondary X-points that form between plasmoids in the collapsing current sheet (Liu et al. 2020). A time history of the reconnection rate $R = (c\, E_{rec})/(v_A\, B_0)$ based on the reconnection electric field E_{rec} is plotted in Figure 1. E_{rec} is computed from the time derivative of the magnetic flux Ψ, which in turn is obtained by calculating the out-of-plane component of the vector potential A_y from B_x and B_z and taking $\Psi = \max(A_y) - \min(A_y)$. Taking the inflow speed v_{in} and the outflow speed $v_{out} \approx v_A$ we find that the reconnection rate is similar to their ratio, i.e., $R \approx v_{in}/v_A$.

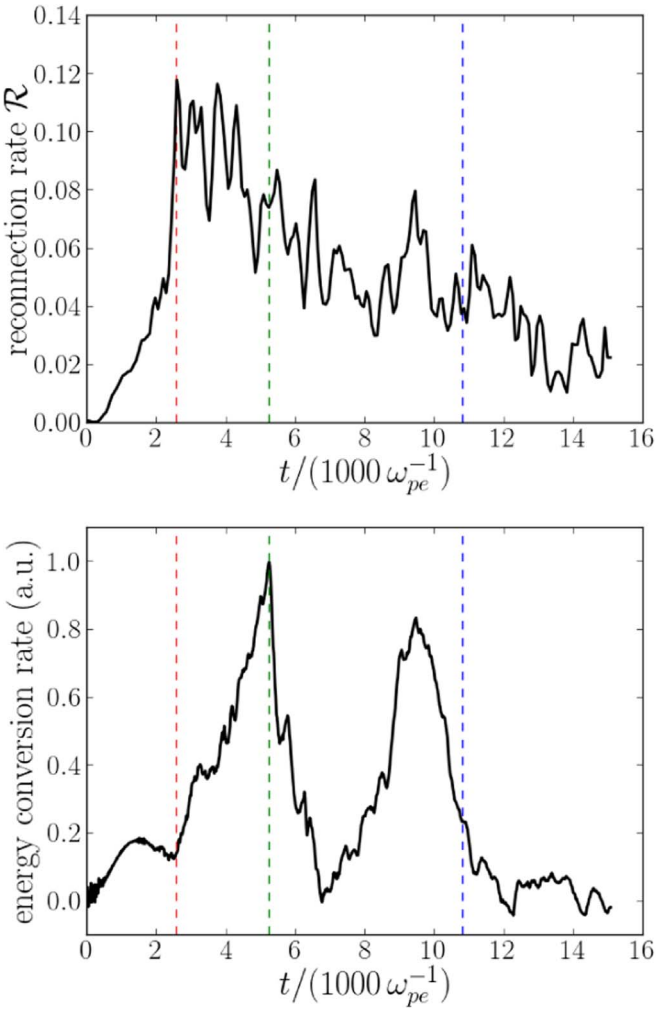

Figure 1. Top: reconnection rate $R = (c\, E_{rec})/(v_A\, B_0)$ based on the reconnection electric field E_{rec}. The vertical lines indicate the three points in time (peak of reconnection rate, peak of energy conversion rate, and reconnection close to saturation) for further analysis. Bottom: rate of magnetic energy conversion in arbitrary units.

Based on the reconnection rate we choose the three points in time in Figure 1 for the analysis presented later in the paper. Figure 2 shows the distribution of current density at the three times. The first point in time is $t_1 = 2572\omega_{pe}^{-1}$. At this time three islands and reconnection outflows from the X-points between them have formed and the reconnection rate peaks. The second point in time that we chose is $t_2 = 5259\omega_{pe}^{-1}$ at the peak of the magnetic energy conversion rate (lower panel in Figure 1). Several islands of different sizes and different spatial separation in the x direction exist and two plasmoids are merging in the middle of the domain, driving a spike in the energy conversion rate as shown in the lower panel in Figure 1. As for the third

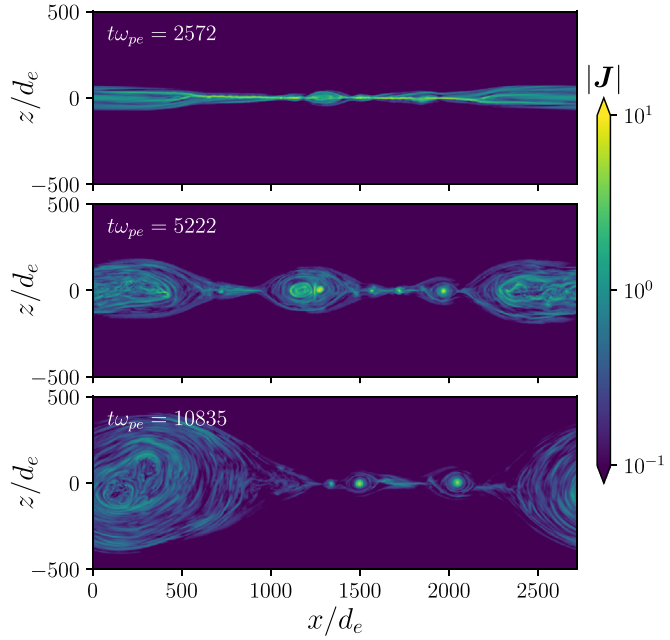

Figure 2. Magnitude of the current density. The three points in time correspond (as closely as output settings allow) to the points in time that are highlighted in Figure 1.

time step we pick $t_3 = 10819\omega_{pe}^{-1}$, which is just short of two Alfvén crossing times. At this point the energy conversion rate and reconnection rate have dropped significantly and the self-interaction of the system via the periodic boundary becomes important.

As mentioned before we employ a reduced but statistically significant number of tracer particles. This allows output at high cadence, including diagnostic quantities that are computed in every time step. The most important quantities used in this paper are the work done by the parallel and perpendicular electric fields, where the directions are split with respect to the local magnetic field at the particle location. The full definition of the two quantities is

$$W_{\parallel}(t) = \frac{q}{m_e\, c^2} \int_0^t \boldsymbol{v}_p(t') \cdot \boldsymbol{E}_{\parallel}(t') dt' \tag{4}$$

$$W_{\perp}(t) = \frac{q}{m_e\, c^2} \int_0^t \boldsymbol{v}_p(t') \cdot \boldsymbol{E}_{\perp}(t') dt' \tag{5}$$

where

$$\boldsymbol{E}_{\parallel}(t') = \frac{\boldsymbol{E}(t') \cdot \boldsymbol{B}(t')}{\boldsymbol{B}(t') \cdot \boldsymbol{B}(t')} \boldsymbol{B}(t') \tag{6}$$

$$\boldsymbol{E}_{\perp}(t') = \boldsymbol{E}(t') - \boldsymbol{E}_{\parallel}(t'). \tag{7}$$

In this definition we use the electric field $\boldsymbol{E}(t)$ at time t at the particle location $\boldsymbol{x}_p(t)$, the magnetic field $\boldsymbol{B}(t)$ at the same time and location, the (negative) electron charge q, electron rest mass m_e, and the electron velocity $\boldsymbol{v}_p(t)$. Since we have a small guide field that avoids magnetic nulls, the decomposition parallel and perpendicular to the magnetic field is meaningful nearly everywhere in the simulation box. The parallel component can only be generated by nonideal, kinetic processes, whereas the perpendicular component can be generated by bulk plasma motion $-\boldsymbol{u} \times \boldsymbol{B}/c$ or the Hall term. The perpendicular component therefore does not require kinetic, nonideal effects. While these nonideal effects can contribute to the perpendicular component, we do not attempt to split the perpendicular component into ideal and nonideal components in this work. Instead, we note that any perpendicular electric field can support Fermi acceleration in a general sense (Lemoine 2019). This is in line with the conclusion that the Fermi acceleration in reconnection is driven by particle curvature drift motions along the perpendicular electric field (Dahlin et al. 2014; Guo et al. 2014; Li et al. 2017).

Figure 3 shows the time history of $W_{\parallel}$, $W_{\perp}$, and $\Delta\gamma$ for four representative tracer particles. The first trajectory (panel a) shows a particle that rapidly gains energy to $\gamma \approx 400$ through the parallel electric field at time $t \approx 8800\omega_{pe}^{-1}$. After this single short episode the particle gains more energy through the perpendicular field over the next $4000\omega_{pe}^{-1}$. This particle trajectory provides evidence that the parallel electric field can provide an "injection" process for further energization through $E_{\perp}$, similar to Ball et al. (2018, 2019). However, inspecting trajectories of the 500 most energetic tracer particles also reveals other acceleration patterns, which are shown in the same figure. The top right trajectory (panel b) shows a particle that never gained appreciable energy from $W_{\parallel}$, but was picked up by $W_{\perp}$ at $t \approx 8100\omega_{pe}^{-1}$ and kept gaining energy more slowly after $\gamma \approx 400$ (Guo et al. 2015; Sironi & Beloborodov 2019). The duration of injection, subsequent acceleration, and final particle energy are very comparable to the previous trajectory, but without appreciable input from $W_{\parallel}$. It is worth noting that the time of injection is also similar to the first particle and coincided with the merger of two large islands.

We also find several trajectories similar to the one displayed in the bottom left corner (panel c), where $W_{\parallel}$ and $W_{\perp}$ have remarkably comparable contributions during the injection. In addition, there are many trajectories that defy simple classification, such as the one shown in the bottom right (panel d) where $W_{\parallel}$ changes sign several times (note that this is integrated work done, not instantaneous power). We also find many trajectories where there is no clear injection moment, but rather a gradual increase in energy over a period of several thousand ω_{pe}^{-1} through a Fermi-like process. This may have important implications, as it suggests that Fermi acceleration does not depend on a real injection process in magnetic reconnection. These trajectories show that the injection process is more complicated than what is shown in Ball et al. (2018, 2019). Therefore more careful future studies on the low-energy acceleration process are desired.

Instead of subjectively classifying trajectories from a limited number of particle trajectories, we resort to statistical quantities computed from all tracer particles. To separate the initial acceleration ("injection") from later particle acceleration (power-law range) we adopt the injection threshold $\gamma_{\rm inj} = \sigma_e/2$ from Ball et al. (2019). For Figure 4 we check in every time step if a tracer has crossed this threshold for the first time and if so we classify it according to the relative contribution of $W_{\parallel}$ and $W_{\perp}$ up to this time. All particles that have exceeded $\gamma_{\rm inj}$ at least once by time t are included in the plot of $N_e(t)$. If a particle falls below the threshold it is not removed from the plot. Neither does its classification change if it is reaccelerated and crosses the threshold again. Note that this disadvantages the perpendicular field that tends to act later than the parallel component of the electric field. We have also repeated the analysis by removing the contribution from particles initially in

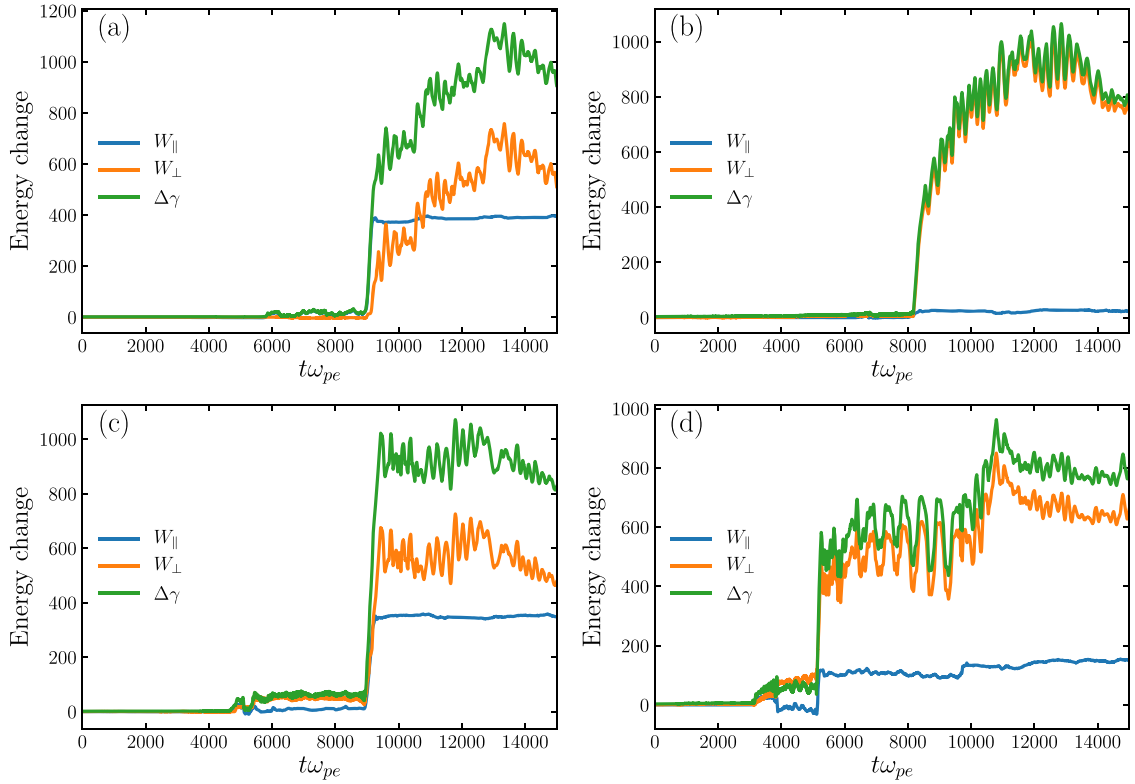

Figure 3. Four electron trajectories. (a) The top left trajectory illustrates the case where a particle is first injected due to $W_\parallel$ and then gains further energy due to $W_\perp$. (b) The second trajectory illustrates that $W_\perp$ can directly inject particles with a negligible contribution from $W_\parallel$. (c) The third trajectory illustrates that both components of the electric field can act simultaneously during injection. (d) The fourth trajectory illustrates that for many particles classification of the injection mechanism is not straightforward.

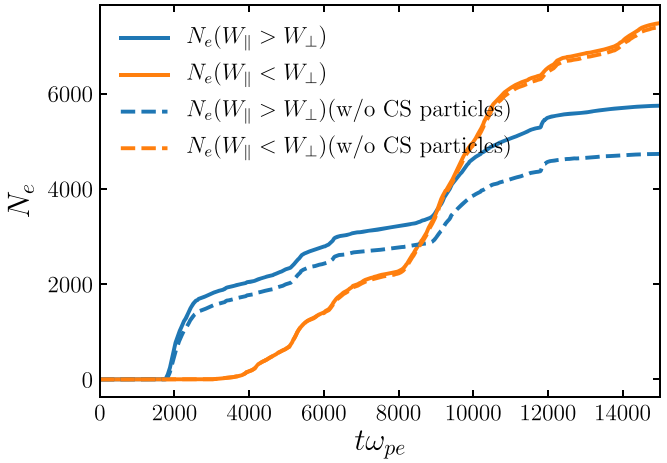

Figure 4. Number of tracer particles that have been injected up to time t and that see a stronger contribution of $W_\parallel$ ($W_\parallel > W_\perp$) or $W_\perp$ ($W_\perp > W_\parallel$) before injection as a function of time t.

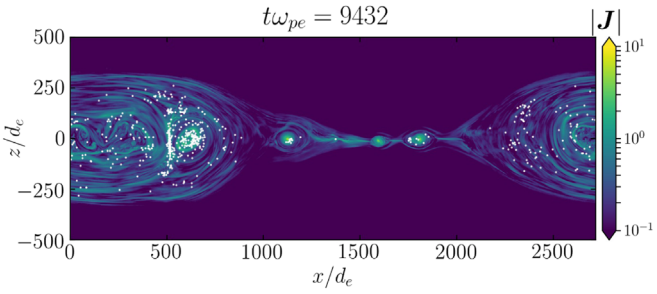

Figure 5. Current density and particle location at $t = 9432\,\omega_{pe}^{-1}$ for particles that cross $\gamma_{\rm inj} = \sigma_e/2$ around that time.

the current sheet and confirmed that they do not modify our conclusion. Plotting the number of particles crossing $\gamma_{\rm inj}$ due to more contributions by the parallel electric field ($W_\parallel > W_\perp$) or perpendicular electric field ($W_\perp > W_\parallel$) as a function of time reveals that both $W_\parallel$ and $W_\perp$ contribute to the injection process. Figure 4 shows that even in a triggered reconnection setup it takes a while for particles to cross $\gamma_{\rm inj}$ even if particles initially in the current sheet are not excluded. The first particles that reached the threshold energy do so due to a dominant contribution from $W_\parallel$. The time delay and the number of particles that first cross $\gamma_{\rm inj}$ likely depend on the details of reconnection onset. Probing this initial phase in a self-consistent way is difficult and requires knowledge about current sheet formation in the specific astrophysical context. A larger simulation shows a smaller initial jump due to $W_\parallel$ and a smoother increase of both curves over time. Later in time, particles typically cross the threshold during episodes of plasmoid mergers. This is especially noticeable from time $t \approx 8500\omega_{pe}^{-1}$ when two large plasmoid mergers start as depicted in Figure 2. Earlier plasmoid mergers at times (4500, 5500, 6800) ω_{pe}^{-1} follow the same trend. Note that both the numbers of particles that reach the threshold with $W_\parallel > W_\perp$ and $W_\parallel < W_\perp$ jump at the same time.

Figure 5 selects all tracer particles that crossed the threshold $\gamma_{\rm inj} = \sigma_e/2$ in the time interval $9393 < t\,\omega_{pe} < 9471$ and shows their location at the middle of the interval on top of the current density at that point in time. Plotting the location of particles as they cross the threshold reveals two preferred locations: the first is secondary current sheets that are formed as

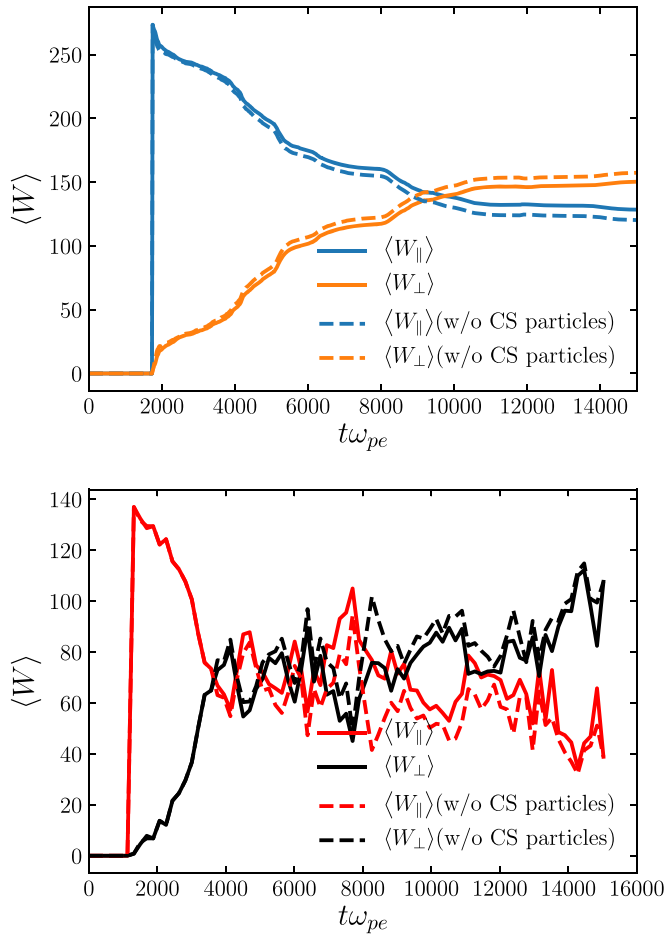

Figure 6. Contributions of the work done by the parallel and perpendicular electric fields to particle injection. Top panel: $W_\parallel$ and $W_\perp$ are averaged over all tracer particles that have crossed the injection threshold by time t. Bottom panel: $W_\parallel$ and $W_\perp$ averaged over all tracer particles that have crossed $\gamma_{\rm inj} = \sigma_e/2$ within the last 100 time steps before time t.

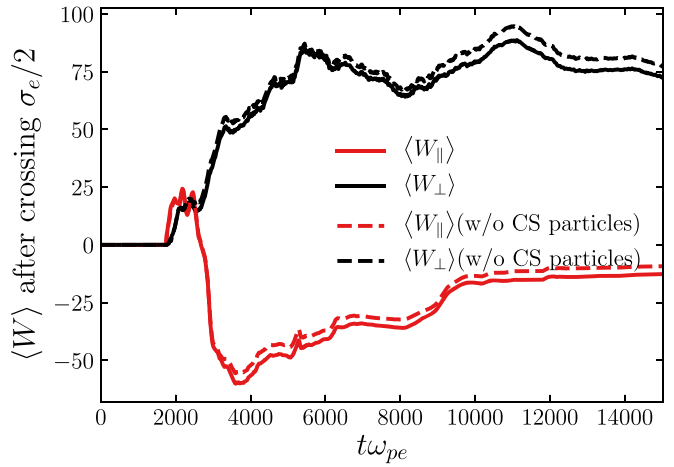

Figure 7. Average energy gain due to parallel and perpendicular electric field of all particles that have already crossed the threshold $\gamma > \sigma/2$ as a function of time. After a very short initial time, energy gain is dominantly due to the perpendicular electric field, while the parallel field removes energy from the particles.

islands merge. Strong nonideal fields are expected at these locations. We still see particles clustering there late in the simulation at $t \sim 10{,}400\,\omega_{pe}^{-1}$ when injection is preferentially done by parallel fields. The other location is the inside of islands as they merge, probably due to the compression of those interacting islands (Du et al. 2018; Li et al. 2018a). At late times more injected particles are due to $W_\perp > W_\parallel$. Note that this effect is not visible at early times. The effect of $W_\perp$ is suppressed for another simulation with half the box size and gets more pronounced when doubling the box size. This is examined and discussed in Appendix A. This might indicate that the effect of $W_\perp$ is underestimated in simulations with smaller domains. However, even with only two spatially resolved dimensions, the simulations are so expensive that scaling up further to a box size relevant to astrophysics is not possible.

Figure 4 counts the number of injected particles due to dominant $W_\perp$ and $W_\parallel$ but does not include the magnitude of $W_\parallel$ and $W_\perp$. To get a measure of the relative contribution of the two, we average both quantities over all tracer particles at the point in time when the tracer particle crosses $\gamma_{\rm inj}$. Note two thing about this plot: the averaging $\langle ... \rangle$ is done over injected particles not over time t. Figures plotted with blue/orange colors show quantities calculated for all particles that are injected by time t using quantities at their injection time $t_{\rm inj} \leqslant t$. This also implies that $W_\parallel + W_\perp = \gamma_{\rm inj}$. Figure 6(a) shows the resulting averages. Figure 6(b) shows how the averages change in time when only considering particles that cross in the last 100 time steps. As in other plots we use red/black for instantaneous quantities. The results are much more noisy due to the limited number of particles available for averaging, but they support the same conclusions.

The initial delay is again visible as well as the fact that the first handful of particles reach $\gamma = \sigma_e/2$ due to $W_\parallel$. Acceleration by the parallel electric field is an effect that occurs in the initial phase of reconnection. As time progresses the influence of the perpendicular fields become more and more visible as additional particles reach the threshold due to work due by the perpendicular field. Late in the simulation, at two Alfvén times ($11{,}300\,\omega_{pe}^{-1}$) the split is about 1.21:1 in favor of $W_\perp$ compared to $W_\parallel$ for particles that started outside the current sheet. For a smaller simulation of half the size, the average contribution of $W_\parallel$ is larger than $W_\perp$. At two Alfvén times the split is about 1:4.29 for $W_\perp$ compared to $W_\parallel$ for particles that are initially outside the current sheet. But for a simulation of twice the size the split improves in favor of $W_\perp$ to about 1.44:1 at two Alfvén times for particles that start outside the current sheet (see Appendix). For both large simulations equal contributions are reached at the same time $t \approx 10{,}000\omega_{pe}^{-1}$.

In addition to the initial energy gain up to $\gamma_{\rm inj}$, we also examine the mechanism of further acceleration that leads to development of the power-law distribution. Figure 7 shows the averaged energy gain from parallel and perpendicular electric fields of all particles with $\gamma > \gamma_{\rm inj}$ as a function of time. The contribution of the perpendicular electric field dominates over the parallel electric field. In fact, for most of the simulation duration high-energy particles lose energy to the parallel electric field and only reach energies significantly above $\gamma_{\rm inj}\, m_e\, c^2$ due to $W_\perp$. This fits well with the established picture of secular, late-time energization through a Fermi-type process (Guo et al. 2014, 2019).

Figure 8 shows the energy spectra of all tracers at intervals of about $780\,\omega_{pe}^{-1}$. Additionally, the spectra at the points in time that are highlighted in Figure 1 are plotted. By time t_1 when the

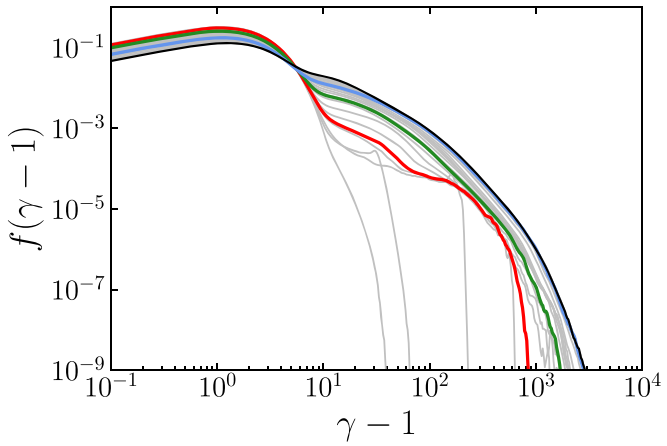

Figure 8. Particle spectra of all tracer electrons at different times. The light gray lines are separated by approximately 780 ω_{pe}^{-1} and the solid colored lines correspond to the times highlighted in Figure 1. The black line shows the energy spectrum at the end of the simulation.

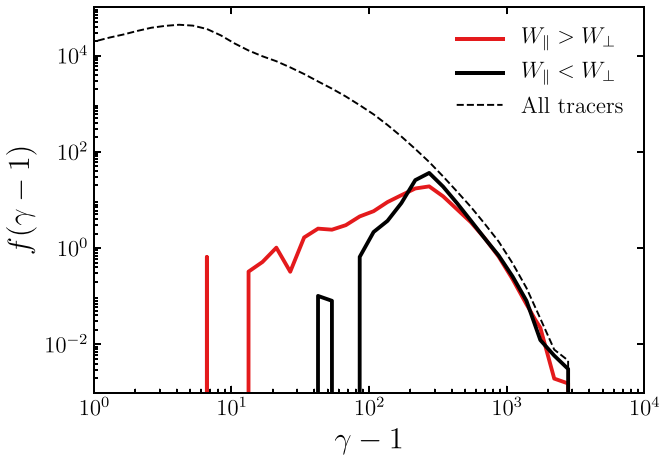

Figure 9. Particle spectrum of electrons that did not start in the current sheet at the end of the simulation, divided according to the work done by the parallel and perpendicular field up to the moment when they cross $\gamma_{\rm inj} = \sigma_e/2$. Particles that do not appreciably lose energy later in the simulation show very similar spectra. Some particles, however, lose their energy at later times, in particular if they originally gain more energy from the parallel field than the perpendicular field.

reconnection rate peaks there are already signs of the heated downstream Maxwellian and a number of nonthermal particles with $\gamma > 100$. A few of them have even reached $\gamma > \sigma_e/2$ already. At time t_2 when the energy conversion rate peaks there are many more particles in the heated downstream. At energies above this heated Maxwellian a power-law distribution with $p \approx 2$ has formed. At the late time t_3 the downstream Maxwellian and the high-energy tail have grown in particle number. The spectrum has reached its final cutoff at $\gamma \approx 1000$ with a few particles extending up to $\gamma \approx 2000$. In the remaining timestep until the end of the simulation some more particles are processed into heated downstream plasma, but the high-energy tail remains unchanged. This might be an artifact of the 2D simulations performed here that prevent energized particles from accessing energization sites that only appear late in the simulation.

Figure 9 shows the energy spectrum of all tracer particles at the end of the simulation. Also plotted are the final spectra of the subpopulations that crossed the injection threshold with $W_\parallel > W_\perp$ or $W_\parallel < W_\perp$. Not all of those particles remain at $\gamma > \sigma_e/2$ until the end of the simulation, but the ones that do stay in the nonthermal high-energy tail exhibit nearly identical spectra, independent of the process that got them across the threshold. This is consistent with all particle acceleration in that energy range coming from $W_\perp$ setting identical spectra, independent of the initial source of particle energy below the threshold. Particles that gain energy through $W_\parallel$ initially might be a bit more likely to lose energy again later, but this effect decreases with simulation size and is not significant.

To further investigate the contribution of $W_\parallel$ and $W_\perp$ to $\Delta\gamma$ we looked for a way to visualize the evolution of all three quantities as a function of time for all tracer particles. Each tracer can be visualized as a point in the three-dimensional $W_\parallel$–$W_\perp$–$\Delta\gamma$ space and moves on the two-dimensional $\Delta\gamma = W_\parallel + W_\perp$ surfaces over time. Figures 10 through 12 show three projections of this three-dimensional space at times t_1, t_2, and t_3 as defined in Figure 1. To visualize the density of the point clouds of all 0.6 million tracers we computed histograms that count the number of points in each bin. All three axis of the three-dimensional space can be positive or negative, but span a large range. We therefore decided to plot the negative and positive halves of each axis on a separate logarithmic scale.

Figure 10 shows the change in Lorentz factor $\Delta\gamma$ versus the work done by the parallel electric field $W_\parallel$. The upper right quadrant in each of the three subplots is basically identical to Figure 10 in Ball et al. (2019). However, the other three quadrants also show interesting features. At early times there is a good correlation between the two quantities, as indicated by the bright feature in the histogram along the $\Delta\gamma = W_\parallel$ line. Note, however, that this feature is mostly located at $\Delta\gamma < \gamma_{\rm inj}$. At later times more particles have reached $\Delta\gamma > \gamma_{\rm inj}$, but there is a systematic shift of the peak of the histogram toward $\Delta\gamma > W_\parallel$. This indicated that there is an additional energy gain due to $W_\perp$. While this shift is visually small (in logarithmic scale), the more quantitative analyses in Figures 4 and 5 have shown the importance of $E_\perp$ during particle injection.

To get a true sense of the role of the perpendicular electric field, it is better to look at Figure 11. At early times there is a surprising correlation between $\Delta\gamma$ and $W_\perp$ at low energies up to maybe $\gamma \approx 10$. At high energies no such correlation is visible. Many particles have more energy than can be explained by $W_\perp$ alone. But as time goes on the correlation between $\Delta\gamma$ and $W_\perp$ improves and extends to higher energies. At late times the correlation extends beyond $\sigma_e/2$ and is better than the correlation with $W_\parallel$.

Figure 12 shows the contributions of both parallel and perpendicular electric fields. The resulting change in Lorentz factor is given by their sum. The threshold $\gamma_{\rm inj}$ is indicated in the plot. The curved nature of this line illustrates how deceptive the double logarithmic presentation can be. At the earliest time t_1 particles cross the threshold $\gamma_{\rm inj} \approx 275$ indeed mostly due to $W_\parallel$. The majority of high-energy particles, however, are close to the line of equal contributions $W_\parallel \approx W_\perp$. There is also a large number of particles that gained energy dominantly due to $W_\perp$ with energies up to $\gamma \approx 15$. As time progresses more particles reach high energies, but increasingly close to $W_\parallel \approx W_\perp$. Some particles even cross the threshold with no, or even a negative, contribution from $W_\parallel$. On the other hand

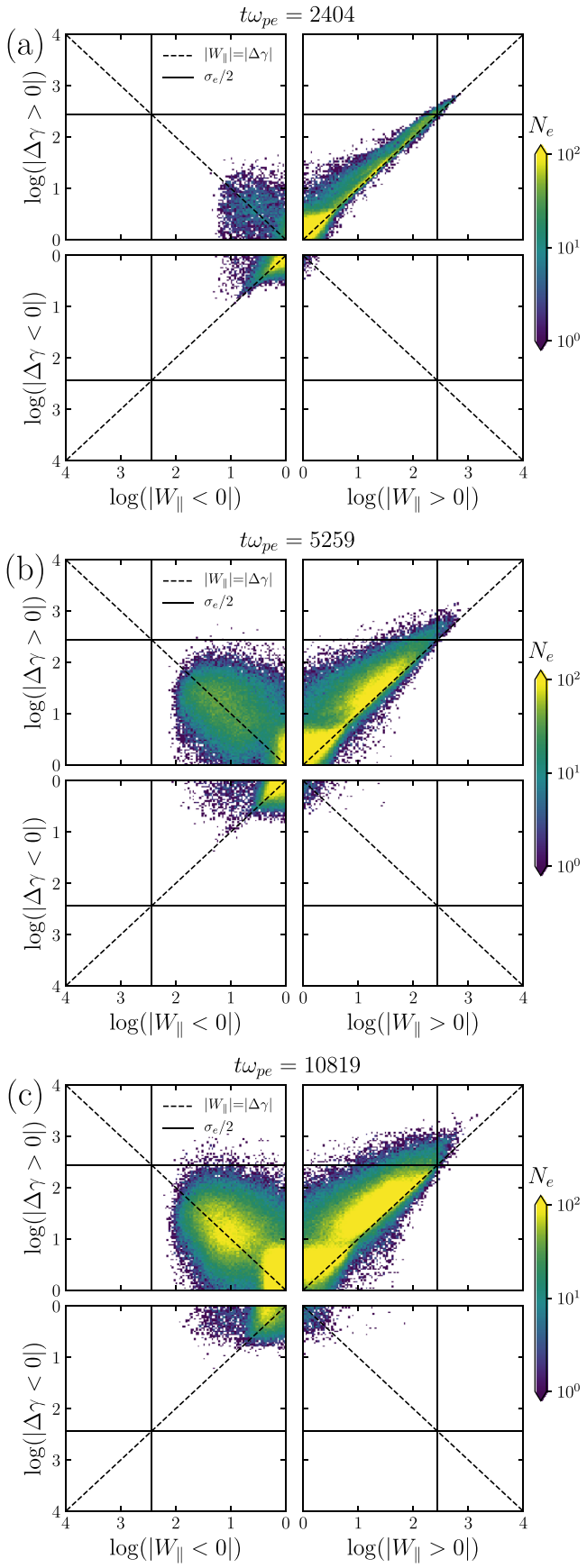

Figure 10. Contribution to energy gain/loss by the parallel electric field on all particles that started outside the current sheet.

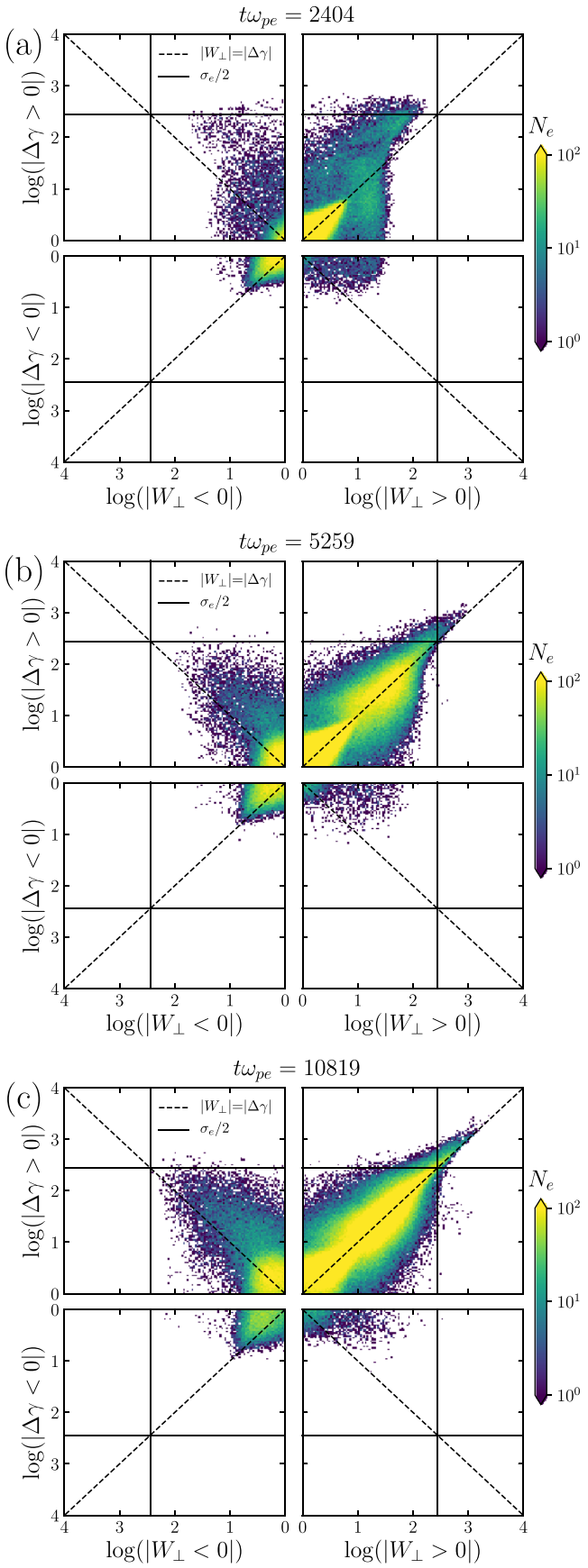

Figure 11. Contribution to energy gain/loss by the perpendicular electric field on all particles that started outside the current sheet.

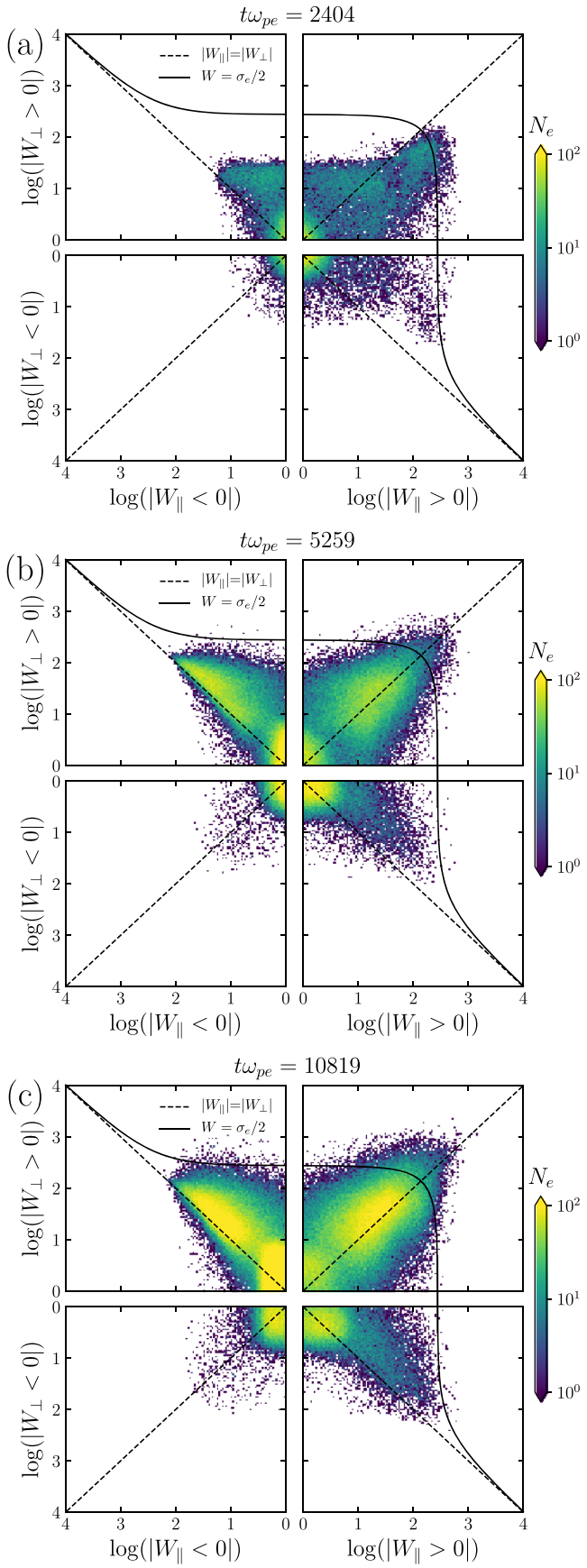

Figure 12. Contribution to energy gain/loss by the parallel/perpendicular electric field on all particles that started outside the current sheet.

there are only a few single particles that reach large energies with no (or negative) contributions from $W_\perp$.

4. Conclusion

The quest for the origin of power-law energy spectra in magnetic reconnection continues, as more careful analyses reveal more physics insights. In this paper we performed fully kinetic simulations of magnetic reconnection using $\sigma_i = 0.3$ and $\sigma_e = 552.5$. While earlier studies in this transrelativistic regime ($\sigma_i < 1 < \sigma_e$) focused on the role of parallel electric field on particle injection (from very low energy to the lower bound $\gamma \sim \sigma_e/2$ of the power-law energy spectra), we study the acceleration by both components of the electric field parallel and perpendicular to the local magnetic field.

We summarize our primary conclusions as follows:

1. The first few particles that reached the injection energy $\gamma \approx \sigma_e/2$ are mostly accelerated by the nonideal electric field that is parallel to the magnetic field. The acceleration by the perpendicular electric field becomes important as the simulation proceeds and eventually outperforms the parallel electric field in terms of particle injection up to the lower-energy bound of nonthermal distribution.
2. The acceleration beyond the low-energy "injection" to high energy is completely dominated by perpendicular electric field acceleration. The resulting power-law energy spectra, no matter whether they are injected primarily by the parallel or perpendicular electric field, resemble each other in terms of the spectral index and the high-energy break. This provides further support for the Fermi acceleration scenario, as the acceleration to power-law energy is not sensitive to the mechanism and spectral form of the injection processes (Guo et al. 2019).
3. In the transrelativistic regime, even low-β plasmas result in relativistic electron thermal speeds that are sufficient for particles to be picked up by a Fermi-type process.[5] This indicates that the threshold for triggering Fermi acceleration is not a major barrier. In fact, we find that some particles can also be accelerated by a Fermi-like process alone, without a clear preceding acceleration. Of course this process is slower, as the Fermi acceleration rate scales with the particle energy and is only visible in sufficiently large simulations. While the parallel electric field may increase the flux of nonthermal particles by providing a preceding acceleration, a perpendicular electric field plays a similar role for particle injection. The energetic particle flux in the simulation will drop significantly without either of the two.

We also repeated the analysis shown in this paper for $\gamma_{\rm inj} = \sigma_e/4$, as shown in Appendix B, but this only leads to minor modification of our results. At high energies $W_\perp$ dominates $W_\parallel$. To get particles up to $\gamma_{\rm inj}$ both $W_\parallel$ and $W_\perp$ can have comparable influence. This is a deviation from the picture that sees $W_\parallel$ acting below $\gamma_{\rm inj}$ and $W_\perp$ above. We conclude that neither of the two should be neglected in the mildly relativistic range where γ is between a few and a sizable fraction of σ_e. The exact balance of $W_\parallel$ and $W_\perp$ depends on many factors, such as the exact choice of $\gamma_{\rm inj}$, system size, and

[5] Sufficiently low plasma β will reduce the electron thermal speed to nonrelativistic values. This is a regime that has not been considered so far.

guide-field strength. In small systems the role of $W_{\parallel}$ may be exaggerated. This may be problematic since simulations of astrophysical extent or even just sufficient size to make robust extrapolations are computationally prohibitively expensive.

Understanding the mechanism of particle injection and further acceleration into a power-law tail allows us to infer the particle spectra in realistic astrophysical systems. Combined with knowledge of the radiation processes it is possible to predict the characteristics of the generated radiation such as spectra, polarization, and light curves (e.g., Zhang et al. 2018). Comparing predictions with observation results allows us to infer the strength, topology, and dynamics of the magnetic fields in astrophysical objects that are otherwise difficult to access. This is of recent interest in the case of radiatively inefficient accretion disks, such as the disks around Sagittarius A* and M87, that have been observed by the Event Horizon Telescope (Chael et al. 2019).

We gratefully acknowledge discussions with David Ball. We acknowledge support by the U.S. Department of Energy (DoE) through the Laboratory Directed Research and Development (LDRD) program at Los Alamos National Laboratory (LANL) and DoE/OFES support to LANL, and NASA ATP program through grant NNH17AE68I. X.L.'s contribution is supported by NASA under grant NNH16AC60I and by the National Science Foundation grant PHY-1902867 through the NSF/DOE Partnership in Basic Plasma Science and Engineering. F.G.'s contributions are in part based upon work supported by the U.S. Department of Energy, Office of Fusion Energy Science, under Award Number DE-SC0018240 and DE-SC0020219. This research was supported by LANL through its Center for Space and Earth Science (CSES). CSES is funded by LANL's LDRD program under project number 20180475DR. This research used resources provided by the LANL Institutional Computing Program, which is supported by the DoE National Nuclear Security Administration under Contract No. 89233218CNA000001.

Appendix A
Influence of the Domain Size

In addition to the nominal simulation with a box size of $L_x \times L_z = 2720\,d_e \times 1360\,d_e$ we also performed simulations with other box sizes to examine how domain size influences injection number and averaged energy gain when particle energy crosses $\gamma_{\rm inj} = \sigma_e/2$.

We performed a *small* simulation with size $L_x' \times L_z' = 1360\,d_e \times 680\,d_e$ using $N_x' \times N_z' = 4096 \times 2048$ grid cells and 167,424 tracer particles among the 8.38×10^8 electrons. Results from this smaller domain size are shown in Figures A1 and A2. Compared to the nominal simulation, a smaller box size leads to an enhancement of $E_{\parallel}$ acceleration and a reduction of the influence of $E_{\perp}$.

We also performed a *square* simulation with size $L_x' \times L_z' = 2720\,d_e \times 2720\,d_e$ using $N_x' \times N_z' = 8192 \times 8192$ grid cells to check for the influence of the upstream boundary conditions. There is a small but noticeable difference in the reconnection rate, in particular at late times, as shown in Figure A3. The number of particles that are injected due to $W_{\parallel}$ and $W_{\perp}$ also change somewhat, as shown in Figure A4. The average energy gain for particles crossing $\gamma_{\rm inj} = \sigma_e/2$ is slightly changed (compare Figure 6(a) with Figure A5). Overall, our main results and conclusions remain unchanged. Because eventually the reconnection outflows still interact with each other via the periodic boundary conditions in the x direction, which reduces reconnection and shuts down particle acceleration, we only show our simulation results until about two Alfvén crossing times.

Finally, we performed a *large* simulation size $L_x'' \times L_z'' = 5440\,d_e \times 2720\,d_e$ using $N_x' \times N_z' = 16384 \times 8192$ grid cells and 655,360 tracer particles among the 1.34×10^{10} electrons. This larger simulation shows an increased influence of $E_{\perp}$ (see Figures A6 and A7). From these simulations we conclude that a larger simulation domain and longer simulation time lead to more important effects for particle injection through $E_{\perp}$.

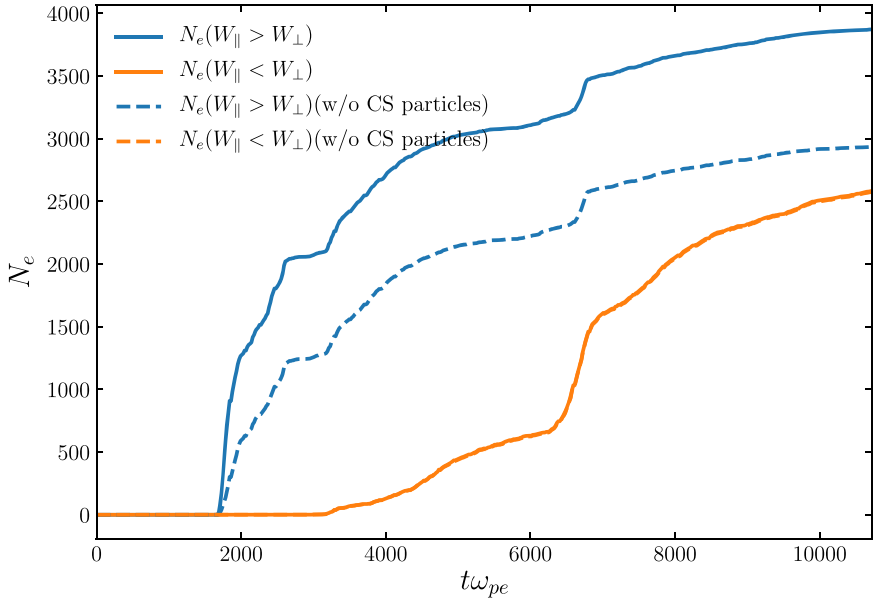

Figure A1. Number of particles dominated by $W_{\parallel}$ or $W_{\perp}$ when crossing $\gamma_{\rm inj} = \sigma_e/2$ in a smaller box of $1360\,d_e \times 680\,d_e$. Analogous to Figure 4.

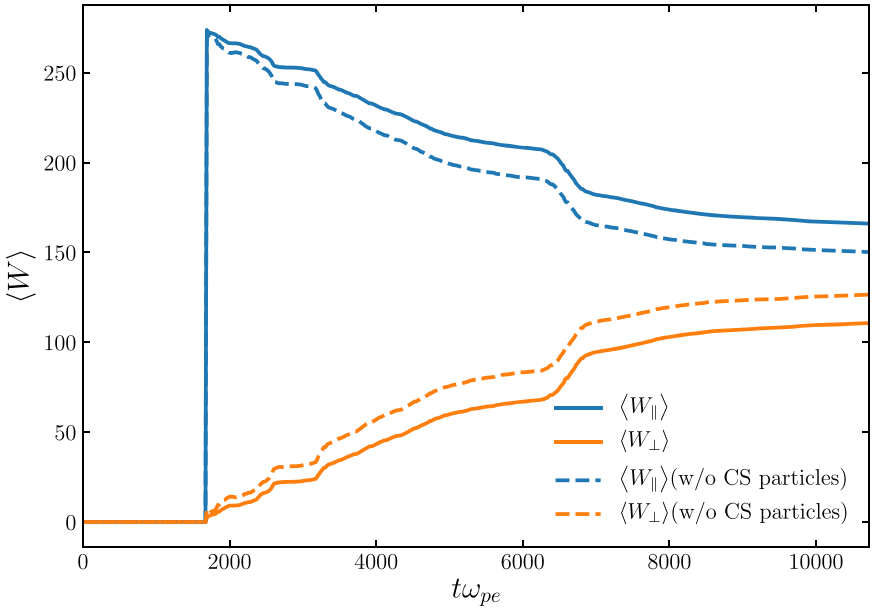

Figure A2. Average energy gain for particles crossing $\gamma_{\rm inj} = \sigma_e/2$ in a smaller box of $1360 d_e \times 680\, d_e$. Analogous to Figure 6.

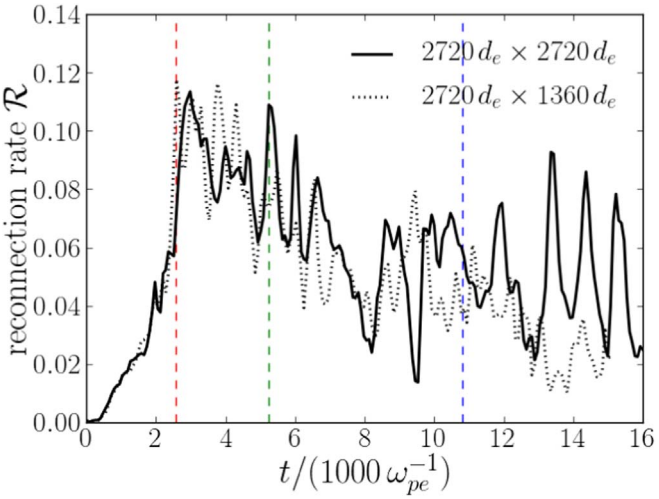

Figure A3. Reconnection rate for $L_z' = 2720\, d_e$. The reconnection rate for the reference simulation that is shown in Figure 1 is included as a dotted line.

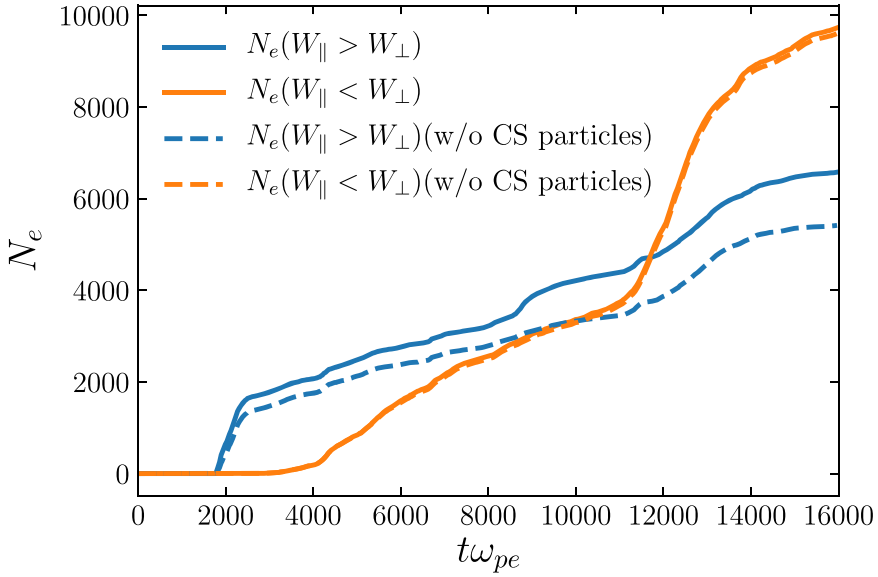

Figure A4. Number of particles crossing $\gamma_{\rm inj} = \sigma_e/2$ for $L_z' = 2720\, d_e$. Analogous to Figure 4.

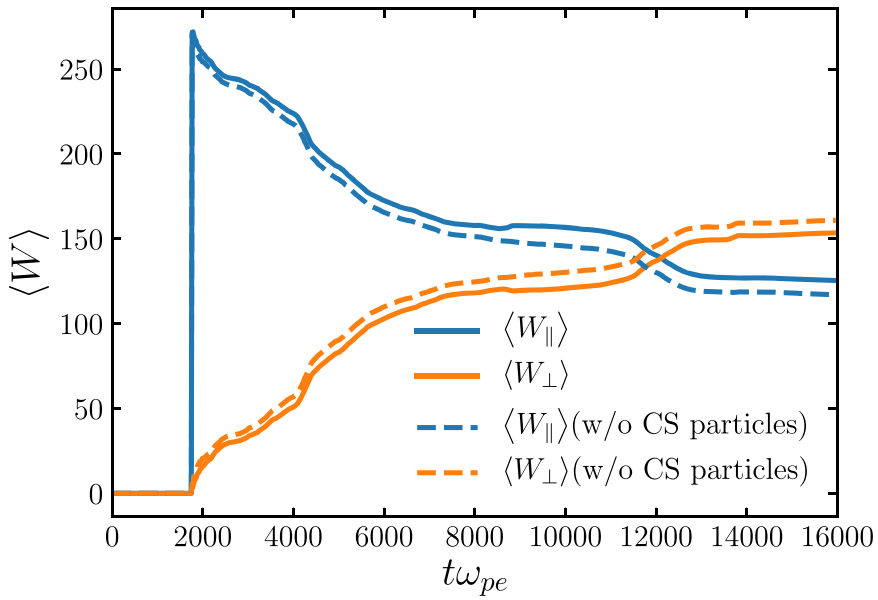

Figure A5. Average energy gain for particles crossing $\gamma_{\rm inj} = \sigma_e/2$ for $L_z' = 2720\, d_e$. Analogous to Figure 6(a).

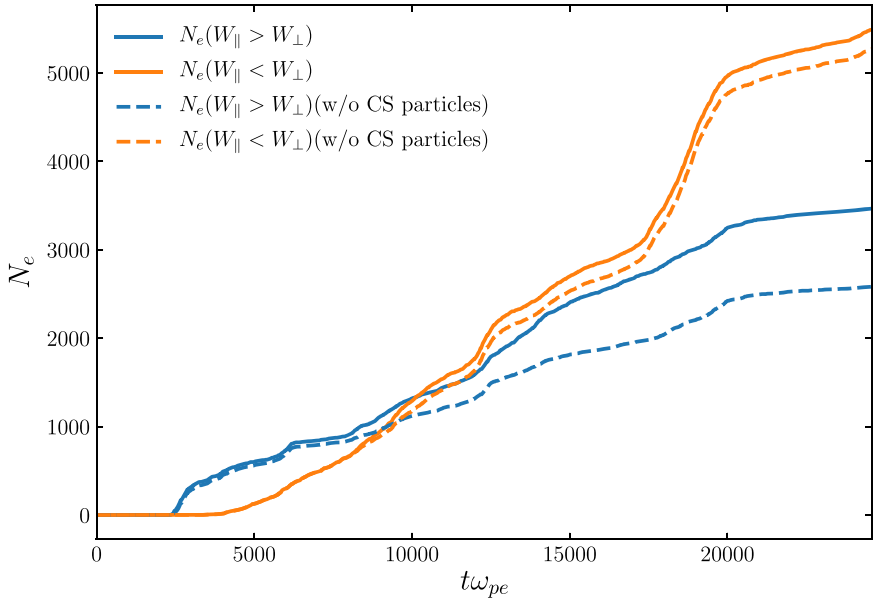

Figure A6. Number of particle dominated by $W_\parallel$ or $W_\perp$ when crossing $\gamma_{\rm inj} = \sigma_e/2$ in a larger box of $5440d_e \times 2720d_e$. Compare with Figures 4 and A1.

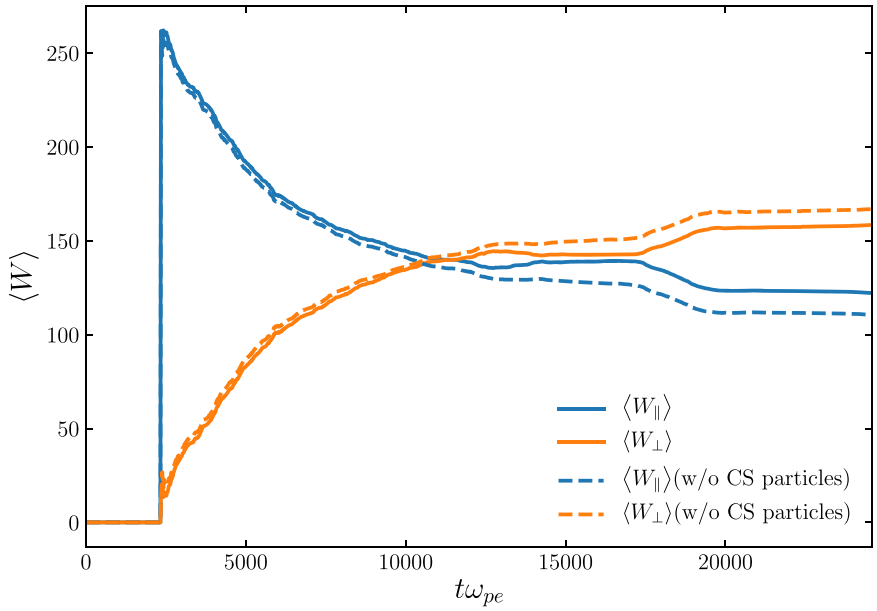

Figure A7. Average energy gain for particles crossing $\gamma_{\rm inj} = \sigma_e/2$ in a larger box of $5440d_e \times 2720d_e$. Compare with Figures 6 and A2.

Appendix B
Influence of the Injection Threshold

We also repeated the analysis shown in the main text for $\gamma_{\rm inj} = \sigma_e/4$. In this appendix we show the two most important plots for the simulation with a box size of $L_x \times L_z = 2720\, d_e \times 1360\, d_e$ from that analysis. Comparing Figure B1 with Figure 4, we see that still injection by $W_\parallel > W_\perp$ is the first process that quickly picks up particles. The time until the first particles crosses the lowered $\gamma_{\rm inj}$ is reduced a little bit. The total number of particles that go over the threshold until the end of the simulation goes up by about a factor of 4. The fact that $W_\parallel > W_\perp$ is important for particles that start inside the current sheet whereas $W_\perp > W_\parallel$ nearly exclusively acts on particles that start outside the current sheet is more pronounced. This leads to the conclusion that for particles outside the current sheet $W_\perp$ is still more important than $W_\parallel$. For particles that start inside the current sheet this is no longer true. Note, however, that the particles that start inside the current sheet are heavily affected by the choice of the initial equilibrium (Harris current sheet versus force-free current sheet) and by the fact that we start with a current sheet that is thin enough to be unstable instead of waiting for the current sheet to thin down dynamically. We therefore are reluctant to make strong claims about those particles. This is consistent with the analysis in Ball et al. (2018), where the authors removed those particles from their analysis.

Compared to Figure 6(a) in the main text, the relative contribution of $W_\perp$ is slightly reduced compared to $W_\parallel$ when the injection threshold is lowered to $\gamma_{\rm inj} = \sigma_e/4$ (shown in Figure B2). For particles that start outside the current sheet it is still (barely) dominant. For earlier times or particles that start inside the current sheet it is slightly smaller. However, in all cases except very early times it is of comparable magnitude and cannot simply be neglected.

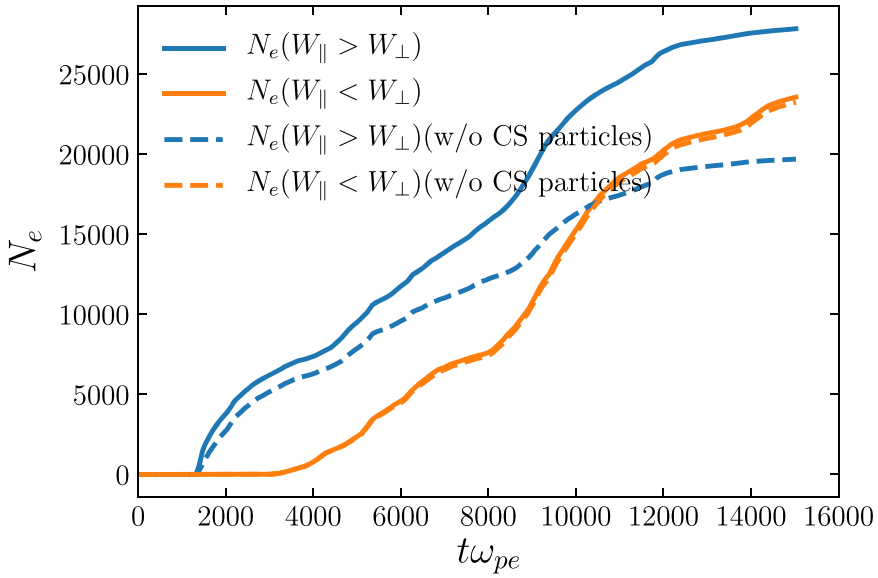

Figure B1. Number of particles crossing the lowered threshold $\gamma_{\rm inj} = \sigma_e/4$. Analogous to Figure 4.

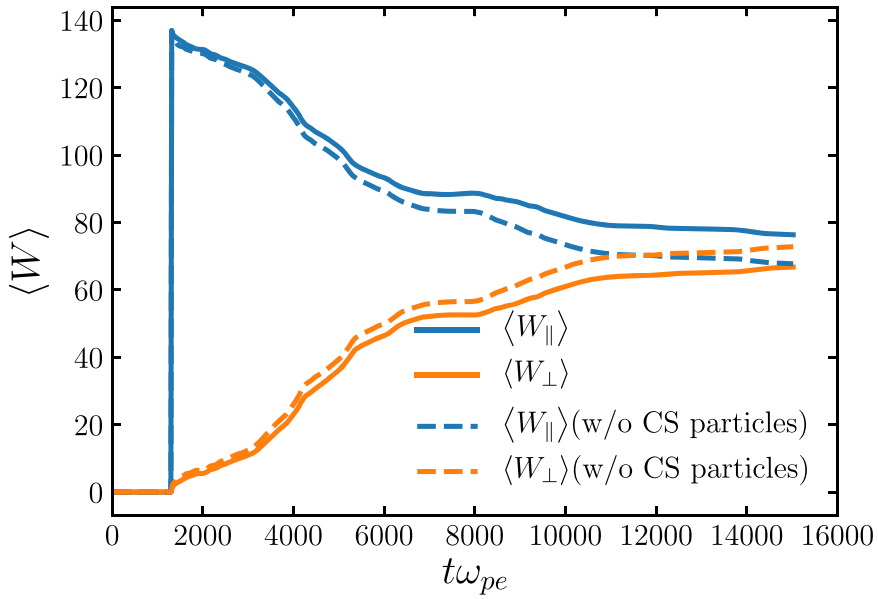

Figure B2. Average energy gain of particles crossing the lowered threshold $\gamma_{\rm inj} = \sigma_e/4$. Analogous to Figure 6(a).

ORCID iDs

Patrick Kilian https://orcid.org/0000-0002-8906-7783
Xiaocan Li https://orcid.org/0000-0001-5278-8029
Fan Guo https://orcid.org/0000-0003-4315-3755
Hui Li https://orcid.org/0000-0003-3556-6568

References

Ball, D., Sironi, L., & Özel, F. 2018, ApJ, 862, 80
Ball, D., Sironi, L., & Özel, F. 2019, ApJ, 884, 57
Birn, J., Drake, J. F., Shay, M. A., et al. 2001, JGR, 106, 3715
Biskamp, D. 1996, Ap&SS, 242, 165
Boris, J. P. 1970, in Proc. Fourth Conference on the Numerical Simulation of Plasmas, ed. J. Boris & R. Shanny (Washington, DC: Naval Research Laboratory), 3
Bowers, K. J., Albright, B. J., Bergen, B., et al. 2008a, in SC '08: Proc. of the 2008 ACM/IEEE Conf. on Supercomputing (Piscataway, NJ: IEEE), 1, https://ieeexplore.ieee.org/document/5222734
Bowers, K. J., Albright, B. J., Yin, L., et al. 2009, JPhCS, 180, 012055
Bowers, K. J., Albright, B. J., Yin, L., Bergen, B., & Kwan, T. J. T. 2008b, PhPl, 15, 055703
Cerutti, B., Werner, G. R., Uzdensky, D. A., & Begelman, M. C. 2013, ApJ, 770, 147
Chael, A., Narayan, R., & Johnson, M. D. 2019, MNRAS, 486, 2873
Chan, C.-K., Psaltis, D., Özel, F., Narayan, R., & Sądowski, A. 2015, ApJ, 799, 1
Dahlin, J. T., Drake, J. F., & Swisdak, M. 2014, PhPl, 21, 092304
Davelaar, J., Bronzwaer, T., Kok, D., et al. 2018, ComAC, 5, 1
de Gouveia dal Pino, E. M., & Lazarian, A. 2005, A&A, 441, 845
di Matteo, T. 1998, MNRAS, 299, L15
Drake, J. F., Swisdak, M., Che, H., & Shay, M. A. 2006, Natur, 443, 553
Drury, L. O. 2012, MNRAS, 422, 2474
Du, S., Guo, F., Zank, G. P., Li, X., & Stanier, A. 2018, ApJ, 867, 16
Fu, X. R., Lu, Q. M., & Wang, S. 2006, PhPl, 13, 012309
Guo, F., Li, H., Daughton, W., & Liu, Y.-H. 2014, PhRvL, 113, 155005
Guo, F., Li, X., Daughton, W., et al. 2019, ApJL, 879, L23
Guo, F., Li, X., Li, H., et al. 2016, ApJL, 818, L9
Guo, F., Liu, Y.-H., Daughton, W., & Li, H. 2015, ApJ, 806, 167
Hesse, M., Kuznetsova, M., & Birn, J. 2001, JGRA, 106, 29831
Lemoine, M. 2019, PhRvD, 99, 083006
le Roux, J. A., Zank, G. P., Webb, G. M., & Khabarova, O. 2015, ApJ, 801, 112
Li, X., Guo, F., Li, H., & Birn, J. 2018a, ApJ, 855, 80
Li, X., Guo, F., Li, H., & Li, G. 2017, ApJ, 843, 21
Li, X., Guo, F., Li, H., & Li, S. 2018b, ApJ, 866, 4
Li, X., Guo, F., Li, H., Stanier, A., & Kilian, P. 2019, ApJ, 884, 118
Liu, Y.-H., Guo, F., Daughton, W., Li, H., & Hesse, M. 2015, PhRvL, 114, 095002
Liu, Y.-H., Hesse, M., Guo, F., et al. 2017, PhRvL, 118, 085101
Liu, Y.-H., Lin, S.-C., Hesse, M., et al. 2020, ApJL, 892, L13
Lyubarsky, Y., & Liverts, M. 2008, ApJ, 682, 1436
Mahlmann, J. F., Levinson, A., & Aloy, M. A. 2020, MNRAS, 494, 4203
Melzani, M., Walder, R., Folini, D., Winisdoerffer, C., & Favre, J. M. 2014a, A&A, 570, A111
Melzani, M., Walder, R., Folini, D., Winisdoerffer, C., & Favre, J. M. 2014b, A&A, 570, A112
Muñoz, P. A., Told, D., Kilian, P., Büchner, J., & Jenko, F. 2015, PhPl, 22, 082110
Nathanail, A., Fromm, C. M., Porth, O., et al. 2020, MNRAS, 495, 1549
Porth, O., Olivares, H., Mizuno, Y., et al. 2017, ComAC, 4, 1
Priest, E., & Forbes, T. 2007, Magnetic Reconnection (Cambridge: Cambridge Univ. Press)
Pritchett, P. L. 2006, JGRA, 111, A10212
Rowan, M. E., Sironi, L., & Narayan, R. 2017, ApJ, 850, 29
Rowan, M. E., Sironi, L., & Narayan, R. 2019, ApJ, 873, 2
Shay, M. A., Drake, J. F., & Swisdak, M. 2007, PhRvL, 99, 155002
Sironi, L., & Beloborodov, A. M. 2019, ApJ, in press (arXiv:1908.08138)
Sironi, L., & Spitkovsky, A. 2014, ApJL, 783, L21
Treumann, R., & Baumjohann, W. 2013, FrP, 1, 31
Wang, H., Lu, Q., Huang, C., & Wang, S. 2016, ApJ, 821, 84
Werner, G. R., Uzdensky, D. A., Begelman, M. C., Cerutti, B., & Nalewajko, K. 2017, MNRAS, 473, 4840
Werner, G. R., Uzdensky, D. A., Cerutti, B., Nalewajko, K., & Begelman, M. C. 2015, ApJL, 816, L8
Yee, K. 1966, ITAP, 14, 302
Zelenyi, L. M., Lominadze, J. G., & Taktakishvili, A. L. 1990, JGR, 95, 3883
Zenitani, S., & Hoshino, M. 2001, ApJL, 562, L63
Zhang, H., Li, X., Guo, F., & Giannios, D. 2018, ApJL, 862, L25